Homogenized descriptions for the elastoplastic response of polycrystalline solids with complex hardening laws: Application to neutron-irradiated bainitic steels

Loïc Chaix, Mihail Garajeu, Pierre-Guy Vincent, Ghiath Monnet, Martín Idiart

Homogenized descriptions for the elastoplastic response of polycrystalline solids with complex hardening laws: application to neutron-irradiated bainitic steels

Loïc Chaix[a,b], Mihail Garajeu[b], Pierre-Guy Vincent[a], Ghiath Monnet[c], Martín I. Idiart[d,e,*]

[a] *Institut de Radioprotection et de Sûreté Nucléaire (IRSN), PSN-RES/SEMIA/LSMA, BP 3, 13115, Saint-Paul-lez-Durance Cedex, France.*

[b] *Aix Marseille Univ, CNRS, Centrale Marseille, LMA UMR 7031, Marseille, France.*

[c] *EDF–R&D, MMC, avenue des Renardières, 77818, Moret sur Loing, France.*

[d] *Centro Tecnológico Aeroespacial/Departamento de Ingeniería Aeroespacial, Facultad de Ingeniería, Universidad Nacional de La Plata, Avda. 1 esq. 47 S/N, La Plata B1900TAG, Argentina.*

[e] *Consejo Nacional de Investigaciones Científicas y Técnicas (CONICET), CCT La Plata, Calle 8 N° 1467, La Plata B1904CMC, Argentina.*

Abstract

Homogenized descriptions are provided for polycrystalline solids deforming in accordance with certain crystal plasticity laws recently proposed for neutron-irradiated bainitic steels. These laws express intragranular plastic slip rates in terms of resolved shear stresses and key microstructural features, such as densities of forest dislocations and of solute clusters, for a wide range of deformation rates, temperatures, and radiation doses. The elastic domain is delimited by thresholds on the resolved stresses that depend on dislocation densities in an intricate manner, and the plastic hardening is described by evolution laws of the Mecking-Kocks type for the dislocation densities with plastic slip. However, thresholds also depend nonlinearly on the resolved stresses themselves. Full-field homogenized descriptions are generated with a Fast Fourier Transform algorithm implemented in the computer code CraFT, while mean-field homogenized descriptions are generated by means of a linear-comparison scheme based on a generalized-secant linearization of the crystal plasticity laws. Multiple ways of accounting for plastic hardening in the mean-field descriptions are explored. Sample results are reported in the form of uniaxial traction curves and concomitant dislocation density evolutions under different scenarios. Overall, the generalized-secant linearization is found to provide an appropriate compromise between precision and mathematical complexity to generate homogenized descriptions for the elastoplastic response of polycrystalline media governed by complex crystal plasticity laws.

Keywords: polycrystals; elastoplasticity; neutron radiation; homogenization

1. Introduction

The elastoplastic behavior of polycrystalline alloys is often described by physically based crystal plasticity laws with complex hardening rules (e.g., Segurado et al., 2018). On the other hand, rigorous mean-field homogenization schemes for up-scaling crystal plasticity laws often neglect elastoplastic interactions and plastic hardening to enable the use of variational approximations (e.g., Dendievel et al., 1990; DeBotton

*Corresponding author

Email addresses: lchaix@lma.cnrs-mrs.fr (Loïc Chaix), mihai.garajeu@univ-amu.fr (Mihail Garajeu), pierre-guy.vincent@irsn.fr (Pierre-Guy Vincent), ghiath.monnet@edf.fr (Ghiath Monnet), martin.idiart@ing.unlp.edu.ar (Martín I. Idiart)

and Ponte Castañeda, 1995; Bornert and Ponte Castañeda, 1998; Liu and Ponte Castañeda, 2004; Ponte Castañeda, 2015). A few strategies to incorporate those features into variational mean-field schemes have been pursued notwithstanding, at the expense of introducing ad-hoc approximations adapted to the particular hardening rule being considered (e.g., Masson et al., 2000; Lebensohn et al., 2007; Suquet and Lahellec, 2014).

The purpose of this work is to adapt a particular mean-field homogenization scheme to crystal plasticity laws of the type proposed by Monnet et al. (2019) for certain neutron-irradiated bainitic steels employed in nuclear reactor pressure vessels. These laws express intragranular plastic slip rates in terms of resolved shear stresses and key microstructural features, such as densities of forest dislocations and of solute clusters, for a wide range of deformation rates, temperatures, and radiation doses. The elastic domain is delimited by thresholds on the resolved stresses that depend on dislocation densities in an intricate manner, and the plastic hardening is described by evolution laws for the dislocation densities with plastic slip of the type proposed by Kocks and Mecking (2003). However, thresholds also depend nonlinearly on the resolved stresses themselves. Mean-field homogenized descriptions are generated here by means of a linear-comparison scheme based on a generalized secant linearization as proposed by Ponte Castañeda (2015). When applied to crystal plasticity laws that derive from a dissipation potential, this scheme exhibits full stationarity with respect to the properties of the linear-comparison polycrystal. The stress-strain-rate relation estimated directly from the linear-comparison polycrystal is thus expected to provide meaningful predictions even when the underlying crystal plasticity law does not derive from a potential. The scheme also delivers estimates for intragranular statistics of the mechanical fields of first and second order. This additional information is required to estimate the evolution of dislocation densities and ensuing plastic hardening. Following common practice, first-order statistics of plastic slip rates are employed. However, three alternative strategies incorporating second-order statistics are explored. Elementary schemes of the Sachs and Taylor type are also considered. Finally, full-field homogenized descriptions are generated with a Fast Fourier Transform-based algorithm implemented in the computer code CraFT of Moulinec and Suquet (1994, 1998). Elementary schemes and full-field descriptions provide references against which the mean-field descriptions can be assessed. To that end, quantitative comparisons are reported in the form of uniaxial traction curves and concomitant dislocation density evolutions under different scenarios.

Throughout the presentation, the symbol ∇ denotes the nabla operator, the symbol "$\cdot$" denotes the scalar product between vectors as well as tensors, the symbols $\otimes$ and $\otimes_s$ denote the tensor product between vectors as well as tensors and its symmetric part, respectively, the symbols $\mathbf{I}$ and $\mathbb{I}$ denote the second-order and fourth-order symmetric identity tensors, $\mathbb{J}$ and $\mathbb{K}$ are the standard fourth-order hydrostatic and shear projection tensors, and the overdot $\dot{(\cdot)}$ denotes time differentiation.

2. The polycrystalline solid model

2.1. Microgeometry

Polycrystals are regarded here as random aggregates of perfectly bonded single crystals or grains. Individual grains are assumed to be of a similar size, much smaller than the specimen size and the scale of variation of the applied loads. Furthermore, the aggregates are assumed to have statistically uniform and ergodic microstructures.

Let the grain orientations within a representative volume element take on a set of N discrete values, characterized by rotation tensors $\mathbf{Q}^{(r)}$ $(r = 1, ..., N)$ relative to a reference system. All grains with a given orientation occupy a disconnected domain $\Omega^{(r)}$ and are collectively referred to as 'phase' r. The domain occupied by the polycrystal is then $\Omega = \cup_{r=1}^{N} \Omega^{(r)}$. Volume averages over the aggregate Ω and over each phase $\Omega^{(r)}$ will be denoted by $\langle\cdot\rangle$ and $\langle\cdot\rangle^{(r)}$, respectively. The domains $\Omega^{(r)}$ can be described by a set of characteristic functions $\chi^{(r)}(\mathbf{x})$, which take the value 1 if the position vector $\mathbf{x}$ is in $\Omega^{(r)}$ and 0 otherwise. In view of the microstructural randomness, the functions $\chi^{(r)}$ are random variables that must be characterized in terms of ensemble averages (Willis, 1983). Due to the assumed statistical uniformity and ergodicity, one-point probabilities can be identified with the volume fractions —or concentrations— $c^{(r)} = \langle\chi^{(r)}(\mathbf{x})\rangle$ of each phase r, two-point probabilities can be identified with the volume averages $\langle\chi^{(r)}(\mathbf{x})\chi^{(s)}(\mathbf{x}')\rangle$, and so on.

2.2. Microscopic elastoplastic response

Grains are assumed to individually deform by multi-glide along K slip systems so that the strain rate at any given point within a crystal with orientation r is given by the additive composition

$$\dot{\boldsymbol{\varepsilon}} = \dot{\boldsymbol{\varepsilon}}^{el} + \sum_{k=1}^{K} \dot{\gamma}^{(r,k)} \boldsymbol{\mu}^{(r,k)}, \tag{1}$$

where the first term refers to an elastic strain rate, and the second term refers to a plastic strain rate that results from dislocation gliding along the K slip systems with Schmid tensors $\boldsymbol{\mu}^{(r,k)} = \mathbf{m}^{(r,k)} \otimes_s \mathbf{n}^{(r,k)}$ defined in terms of the unit normals $\mathbf{n}^{(r,k)} = \mathbf{Q}^{(r)}\mathbf{n}^{(k)}$ and glide directions $\mathbf{m}^{(r,k)} = \mathbf{Q}^{(r)}\mathbf{m}^{(k)}$. For simplicity, the elastic response is assumed linear and isotropic (Monnet et al., 2019), so

$$\dot{\boldsymbol{\varepsilon}}^{el} = \mathbb{S}\dot{\boldsymbol{\sigma}} \quad \text{with} \quad \mathbb{S} = \frac{1}{3\kappa}\mathbb{J} + \frac{1}{2\mu}\mathbb{K}, \tag{2}$$

where $\boldsymbol{\sigma}$ is the Cauchy stress tensor, and κ and μ are the bulk and shear moduli of the crystal, respectively. The elastic response is therefore spatially homogeneous. It is emphasized that elastic anisotropy could be easily accommodated by all the homogenized descriptions considered below but would not alter the conclusions of this study. The plastic response, on the other hand, is strongly nonlinear and anisotropic. The shear rate along any given system is taken of the peculiar form (Monnet et al., 2019)

$$\dot{\gamma}^{(r,k)} = \dot{\gamma}_0 \sinh\left(\sqrt{\frac{\tau_+^{(r,k)}}{\tau_0}}\right) \operatorname{sgn}(\boldsymbol{\sigma} \cdot \boldsymbol{\mu}^{(r,k)}), \tag{3}$$

where $\dot{\gamma}_0$ and τ_0 denote a reference strain rate and stress, respectively, and $\tau_+^{(r,k)}$ is an effective stress that depends non-linearly on the resolved shear stress $\boldsymbol{\sigma} \cdot \boldsymbol{\mu}^{(r,k)}$ through the equation

$$\tau_+^{(r,k)} = \left[|\boldsymbol{\sigma} \cdot \boldsymbol{\mu}^{(r,k)}| - \tau_c^{(r,k)}(\tau_+^{(r,k)}) \right]_+, \tag{4}$$

where $[\cdot]_+ = \max\{\cdot, 0\}$ denote the Macaulay brackets. In this last expression, $\tau_c^{(r,k)}(\tau_+^{(r,k)})$ is a critical stress level that depends on $\tau_+^{(r,k)}$ as

$$\tau_c^{(r,k)}(\tau_+^{(r,k)}) = \tau_{HP} + \sqrt{\tau_{SC}^2 + \tau_{self}^{(r,k)^2} + \beta \left[\tau_{obs}^{(r,k)} - \tau_+^{(r,k)} \right]_+^2}, \tag{5}$$

where β is a non-dimensional parameter introduced for numerical purposes, while

$$\tau_{HP} = \tau_{cr} \left(\frac{d}{d_0} \right)^{-1/2} \quad \text{and} \quad \tau_{SC} = \tau_{cr} \left(\frac{c_{SC}}{c_{SC0}} \right)^{4/7} \tag{6}$$

are, respectively, characteristic stresses due to the Hall-Petch effect and the presence of solute clusters produced by the neutron radiation. These stresses are proportional to a reference critical stress τ_{cr}, and depend on ferrite lath package size d and solute cluster concentration c_{SC}; d_0 and c_{SC0} are characteristic values for these quantities. In turn,

$$\tau_{self}^{(r,k)} = \tau_{cr} \left(a^{(k,k)} \frac{\rho^{(r,k)}}{\rho_0} \right)^{1/2} \quad \text{and} \quad \tau_{obs}^{(r,k)} = \tau_{cr} \left(\sum_{\substack{k'=1 \\ k' \neq k}}^{K} a^{(k,k')} \frac{\rho^{(r,k')}}{\rho_0} \right)^{1/2} \tag{7}$$

are, respectively, stresses due to the dipolar interactions between dislocations belonging to the same slip system and to different slip systems as characterized by the interaction matrix $a^{(k,k')}$ and a characteristic

k	1	2	3	4	5	6	7	8	9	10	11	12
1	c_1	c_2	c_2	c_1	c_1	c_1	c_1	c_1	c_1	c_1	c_1	c_1
2		c_1	c_2	c_1	c_1	c_1	c_1	c_1	c_1	c_1	c_1	c_1
3			c_1	c_1	c_1	c_1	c_1	c_1	c_1	c_1	c_1	c_1
4				c_1	c_2	c_2	c_1	c_1	c_1	c_1	c_1	c_1
5					c_1	c_2	c_1	c_1	c_1	c_1	c_1	c_1
6						c_1	c_1	c_1	c_1	c_1	c_1	c_1
7							c_1	c_2	c_2	c_1	c_1	c_1
8								c_1	c_2	c_1	c_1	c_1
9									c_1	c_1	c_1	c_1
10										c_1	c_2	c_2
11											c_1	c_2
12												c_1

Table 1: Interaction matrix for the $\langle 111\rangle\{110\}$ slip familly

dislocation density ρ_0. The densities of dislocations $\rho^{(r,k)}$ belonging to each slip system, in turn, evolve with slip according to a classical Kocks-Mecking law of the form (Kocks and Mecking, 2003)

$$\dot{\rho}^{(r,k)} = |\dot{\gamma}^{(r,k)}|\ \rho_0 \left[\left(A_d \frac{d}{d_0} \right)^{-1} + \left(A_{SC} \frac{c_{SC}}{c_{SC0}} \right)^{4/7} + \left(A_{self} a^{(k,k)} \frac{\rho^{(r,k)}}{\rho_0} \right)^{1/2} + \left(\sum_{\substack{k'=1 \\ k' \neq k}}^{K} A_{obs} a^{(k,k')} \frac{\rho^{(r,k')}}{\rho_0} \right)^{1/2} - A_{dis} \frac{\rho^{(r,k)}}{\rho_0} \right] \tag{8}$$

with non-dimensional coefficients A_d, A_{SC}, A_{self}, A_{obs} and A_{dis} characterizing different interaction statistics.

2.3. Macroscopic elastoplastic response

The macroscopic response of the polycrystalline solid is defined as the relation between the time histories of the average strain $\overline{\boldsymbol{\varepsilon}}(t) = \langle \boldsymbol{\varepsilon}(\mathbf{x}, t) \rangle$ and average stress $\overline{\boldsymbol{\sigma}}(t) = \langle \boldsymbol{\sigma}(\mathbf{x}, t) \rangle$ over the representative volume element and a given time interval $0 \leq t \leq T$ (e.g., Michel and Suquet, 2004). Typically, the macroscopic response is determined by prescribing one of the time histories and computing the other. If $\overline{\boldsymbol{\varepsilon}}(t)$ is prescribed, $\overline{\boldsymbol{\sigma}}(t)$ must be computed by averaging the stress field that results from solving the field equations for the displacement field $\mathbf{u}(\mathbf{x}, t)$ within the representative volume element with affine boundary conditions, integrated over time from a certain initial state. Specifically, the field equations are

$$\nabla \cdot \boldsymbol{\sigma} = \mathbf{0}, \quad \dot{\boldsymbol{\varepsilon}} = \nabla \otimes_s \dot{\mathbf{u}}, \quad \dot{\mathbf{u}} = \dot{\overline{\boldsymbol{\varepsilon}}} \mathbf{x} + \dot{\mathbf{u}}', \tag{9}$$

where $\boldsymbol{\sigma}$ and $\dot{\boldsymbol{\varepsilon}}$ must satisfy the constitutive relations spelled out in the previous subsection, and $\mathbf{u}'$ is a displacement field that vanishes on the boundary of the representative volume element. The internal state of the solid is characterized by the collection of $N \times K$ dislocation density fields $\{\rho^{(r,k)}\}$, which play the role of internal variables evolving with a law of the form (8). The total dislocation density within the representative volume element is then given by

$$\overline{\rho}(t) = \sum_{r=1}^{N} \sum_{k=1}^{K} c^{(r)} \langle \rho^{(r,k)}(\mathbf{x}, t) \rangle^{(r)}. \tag{10}$$

2.4. Material parameters for untextured bainitic steels at low temperatures

The present study is restricted to untextured equi-axed polycrystals. Thus, volume fractions are set to $c^{(r)} = 1/N$, multi-point probabilities are assumed isotropic functions of relative positions within the representative volume element, and rotation tensors $\mathbf{Q}^{(r)}$ are specified in terms of Euler angles set in accordance

symbol	parameter	value	unit
κ	bulk modulus	175	GPa
μ	shear modulus	81	GPa
$\dot{\gamma}_0$	reference slip rate	6.3×10^{-16}	s^{-1}
τ_0	reference viscous shear stress	94	kPa
τ_{cr}	reference critical shear stress	300	MPa
d/d_0	ferrite lath package size parameter	8.3	–
ρ_0	characteristic dislocations density	2.24 10^{14}	m^{-2}
A_d	grain size obstacle	0.015	–
A_{SC}	solute clusters obstacle	94.8	–
A_{self}	dislocation obstacle (same system)	11.9	–
A_{obs}	dislocation obstacle (different systems)	107.4	–
A_{dis}	thermal activation and anhilation parameter	5.93	–
c_1	interaction matrix coefficient	0.1	–
c_2	interaction matrix coefficient	0.7	–

Table 2: Material parameters

with a Sobol sequence of N entries (e.g., Lebensohn et al., 2011). The number of grain orientations is set to $N = 100$. The above crystal plasticity law pertains to neutron-irradiated bainitic steels deforming at subfreezing temperatures. Thus, crystals are assumed to glide along the twelve slip systems $\langle 111 \rangle \{110\}$ ($K = 12$) and numerical values for the various material parameters are taken from the works of Monnet et al. (2019) and Chaix (2023) for -100°C and are quoted in Tables 1 & 2. The ratio c_{SC}/c_{SC0}, in turn, is set in Section 5 below for specific radiation doses. Material behavior at such low temperatures is particularly relevant for characterizing ductile-to-brittle transitions (e.g., Chakraborty and Biner, 2014). Finally, the original law of Monnet et al. (2019) defines the critical stress (5) with $\beta = 1$, but the lower value $\beta = 0.7$ is adopted here to ease numerical computations. In this connection, it is noted that expression (5) produces a critical stress level that varies with resolved shear stress from an initial value

$$\tau_c^{(r,k)} = \tau_{HP} + \sqrt{\tau_{SC}^2 + \tau_{self}^{(r,k)^2} + \beta \tau_{obs}^{(r,k)^2}} \tag{11}$$

to a saturation value

$$\tau_c^{(r,k)} = \tau_{HP} + \sqrt{\tau_{SC}^2 + \tau_{self}^{(r,k)^2}}. \tag{12}$$

Thus, the incremental response is independent of the coefficient β deep in the plastic range.

3. Full-field descriptions based on a Fast Fourier Transform algorithm

Full-field descriptions for the above polycrystalline solids are generated here by regarding them as periodic media with unit cells of cubic shape and sufficient microgeometrical intricacy. Granular morphologies are generated by Voronoi tessellations with $N = 100$ seeds distributed in such a way as to optimize uniformity of volume fractions among grains. Each grain is then randomly assigned one of the crystal orientations of the Sobol sequence. Figure 1 shows ten unit cells with different microgeometries.

Following Moulinec and Suquet (1994), the equilibrium equations of Section 2.3, with the crystal plasticity law of Section 2.2 and periodicity conditions on $\mathbf{u}'$, are then discretized in time and space, and solved by a fixed-point method using an implicit Euler scheme and a Fast Fourier Transform algorithm with a cubic grid as implemented in the computer code CraFT. The so-called 'basic' scheme of the code allowing for mixed loading conditions is employed to ensure strain compatibility.

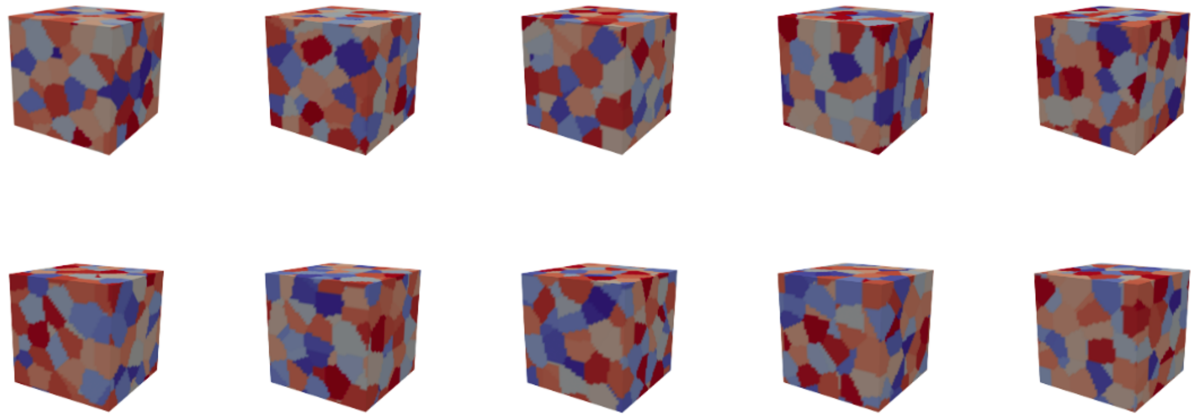

Figure 1: Ten microgeometries employed for the full-field descriptions.

4. Mean-field descriptions

Mean-field descriptions for the above polycrystalline solids are confected here by resorting to two simplifying approximations of common use. Firstly, the homogenization operation on the elastoplastic response is carried out in a decoupled fashion wherein the elastic and plastic deformations are treated separately. Secondly, the dislocation density fields are assumed uniform within all grains with a given orientation r. To expound the rationale behind these approximations, the elastoplastic strain rate (1) at a given instant of the deformation process within any given crystal with orientation r is written as

$$\dot{\boldsymbol{\varepsilon}} = \frac{\dot{\sigma}_m}{3\kappa}\mathbf{I} + \frac{1}{2\mu}\dot{\boldsymbol{\sigma}}_d + \sum_{k=1}^{K} \dot{\gamma}^{(r,k)}\left(\boldsymbol{\sigma}_d \cdot \boldsymbol{\mu}^{(r,k)}, \{\rho^{(r,k)}\}\right)\boldsymbol{\mu}^{(r,k)} \tag{13}$$

where $\sigma_m = \mathrm{tr}\boldsymbol{\sigma}/3$ and $\boldsymbol{\sigma}_d = \boldsymbol{\sigma} - \sigma_m\mathbf{I}$ are the mean and deviatoric parts of the stress, respectively, and the functions $\dot{\gamma}^{(r,k)}$ give the plastic slip rates in terms of the resolved shear stresses and dislocation densities $\{\rho^{(r,k)}\}$ by the constitutive relations (3)-(7). The concomitant evolution laws for the dislocation densities are in turn written as

$$\dot{\rho}^{(r,k)} = \left|\dot{\gamma}^{(r,k)}\left(\boldsymbol{\sigma}_d \cdot \boldsymbol{\mu}^{(r,k)}, \{\rho^{(r,k)}\}\right)\right| \; R^{(k)}\left(\left\{\rho^{(r,k)}\right\}\right), \tag{14}$$

where the functions $R^{(k)}$ are defined by the right-hand side of (8).

Expression (13) is now averaged over the representative volume element to obtain the macroscopic strain-rate-stress relation

$$\dot{\overline{\boldsymbol{\varepsilon}}} = \frac{\dot{\overline{\sigma}}_m}{3\kappa}\mathbf{I} + \frac{1}{2\mu}\dot{\overline{\boldsymbol{\sigma}}}_d + \dot{\overline{\mathbf{E}}}\left[\boldsymbol{\sigma}_d, \left\{\rho^{(r,k)}\right\}\right] \tag{15}$$

with

$$\dot{\overline{\mathbf{E}}}\left[\boldsymbol{\sigma}_d, \left\{\rho^{(r,k)}\right\}\right] = \sum_{r=1}^{N}\sum_{k=1}^{K} c^{(r)}\left\langle \dot{\gamma}^{(r,k)}\left(\boldsymbol{\sigma}_d \cdot \boldsymbol{\mu}^{(r,k)}, \{\rho^{(r,k)}\}\right)\boldsymbol{\mu}^{(r,k)}\right\rangle^{(r)}. \tag{16}$$

Then, the macroscopic strain-rate-stress relation (15) is approximated by a similar relation but with the *functional* (16) replaced by the *function*

$$\dot{\tilde{\mathbf{E}}}\left(\overline{\boldsymbol{\sigma}}_d, \left\{\overline{\rho}^{(r,k)}\right\}\right) = \sum_{r=1}^{N}\sum_{k=1}^{K} c^{(r)}\left\langle \dot{\gamma}^{(r,k)}\left(\boldsymbol{\sigma}_d \cdot \boldsymbol{\mu}^{(r,k)}, \{\overline{\rho}^{(r,k)}\}\right)\boldsymbol{\mu}^{(r,k)}\right\rangle^{(r)}, \tag{17}$$

where the pointwise varying fields $\rho^{(r,k)}$ have been replaced by the piecewise uniform fields $\sum_{r=1}^{N}\chi^{(r)}(\mathbf{x})\overline{\rho}^{(r,k)}$, the deviatoric stress field $\boldsymbol{\sigma}_d(\mathbf{x})$ is now solution to the equilibrium equations in an *elastically rigid* polycrystal with $\langle\boldsymbol{\sigma}_d\rangle=\overline{\boldsymbol{\sigma}}_d$ and intraphase isochoric strain rates given by the averaged terms in (16), and the dislocation densities evolve with some approximation of (14) in terms of piecewise uniform slip-rate measures $\sum_{r=1}^{N}\chi^{(r)}(\mathbf{x})\dot{\overline{\Gamma}}^{(r,k)}$, to be suitably chosen, according to

$$\dot{\overline{\rho}}^{(r,k)}=\dot{\overline{\Gamma}}^{(r,k)}R^{(k)}\left(\left\{\overline{\rho}^{(r,k)}\right\}\right). \tag{18}$$

Approximate stress-strain-rate relations can now be generated by estimating the function (17) with nonlinear homogenization schemes for N-phase media. These schemes can also deliver estimates for the first and second moments of the intraphase field distributions. Estimates for the first and second moments of the intraphase plastic slips can thus be employed in the choice of slip-rate measures for the evolution of the dislocation densities. On the other hand, it is noted that the approximation (17) entails a separate treatment of elastic and plastic deformations in the homogenization process; mean-field descriptions based on this decoupling approximation are therefore unable to provide rigorous intragranular statistics of the strain and stress fields (e.g., Idiart and Lahellec, 2016; Zecevic and Lebensohn, 2020).

4.1. Elementary schemes of the Sachs and Taylor type

Elementary schemes provide simple references against which other schemes can be compared. The elementary scheme of the Sachs type amounts to evaluating the function (17) and concommitant evolution law (18) at a uniform stress field given by its macroscopic value $\overline{\boldsymbol{\sigma}}_d$. Thus, the function (17) is approximated by

$$\dot{\widetilde{\mathbf{E}}}_S\left(\overline{\boldsymbol{\sigma}}_d,\left\{\overline{\rho}^{(r,k)}\right\}\right)=\sum_{r=1}^{N}\sum_{k=1}^{K}c^{(r)}\dot{\gamma}^{(r,k)}\left(\overline{\boldsymbol{\sigma}}_d\cdot\boldsymbol{\mu}^{(r,k)},\{\overline{\rho}^{(r,k)}\}\right)\boldsymbol{\mu}^{(r,k)}, \tag{19}$$

and the slip-rate measures in (18) are identified with

$$\dot{\overline{\Gamma}}_S^{(r,k)}=\left|\dot{\gamma}^{(r,k)}\left(\overline{\boldsymbol{\sigma}}_d\cdot\boldsymbol{\mu}^{(r,k)},\{\overline{\rho}^{(r,k)}\}\right)\right|. \tag{20}$$

In turn, the elementary scheme of the Taylor type amounts to evaluating the function (17) and concommitant evolution law (18) at a uniform plastic strain field. Thus, the function (17) is in this case approximated by a function $\dot{\widetilde{\mathbf{E}}}_T(\overline{\boldsymbol{\sigma}}_d,\{\overline{\rho}^{(r,k)}\})$ defined through the system of algebraic equations

$$\sum_{r=1}^{N}c^{(r)}\overline{\boldsymbol{\sigma}}_d^{(r)}=\overline{\boldsymbol{\sigma}}_d\quad\text{and}\quad\sum_{k=1}^{K}\dot{\gamma}^{(r,k)}\left(\overline{\boldsymbol{\sigma}}_d^{(r)}\cdot\boldsymbol{\mu}^{(r,k)},\{\overline{\rho}^{(r,k)}\}\right)\boldsymbol{\mu}^{(r,k)}=\dot{\widetilde{\mathbf{E}}}_T\quad r=1,...,N, \tag{21}$$

for the function value $\dot{\widetilde{\mathbf{E}}}_T$ and the average deviatoric stresses $\overline{\boldsymbol{\sigma}}_d^{(r)}$, and the slip-rate measures in (18) are identified with

$$\dot{\overline{\Gamma}}_T^{(r,k)}=\left|\dot{\gamma}^{(r,k)}\left(\overline{\boldsymbol{\sigma}}_d^{(r)}\cdot\boldsymbol{\mu}^{(r,k)},\{\overline{\rho}^{(r,k)}\}\right)\right|. \tag{22}$$

4.2. A linear-comparison scheme of the Self-Consistent type

Elementary schemes of the Sachs and Taylor type depend on intragranular field statistics of first order only. To improve accuracy, refined schemes incorporate statistics of second order. In this work we employ the fully optimized second-order homogenization scheme of Ponte Castañeda (2015). This scheme approximates the function (17) by

$$\dot{\widetilde{\mathbf{E}}}_{FOSO}\left(\overline{\boldsymbol{\sigma}}_d,\left\{\overline{\rho}^{(r,k)}\right\}\right)=\widetilde{\mathbb{M}}\left(\overline{\boldsymbol{\sigma}}_d,\left\{\overline{\rho}^{(r,k)}\right\}\right)\overline{\boldsymbol{\sigma}}_d+\widetilde{\boldsymbol{\eta}}\left(\overline{\boldsymbol{\sigma}}_d,\left\{\overline{\rho}^{(r,k)}\right\}\right), \tag{23}$$

where the tensor functions $\widetilde{\mathbb{M}}$ and $\widetilde{\boldsymbol{\eta}}$ represent the effective properties of a linear-comparison polycrystal with the same microgeometry as the original polycrystal but with linear local responses of the form $\dot{\boldsymbol{\varepsilon}}_d = \mathbb{M}^{(r)}\boldsymbol{\sigma}_d + \boldsymbol{\eta}^{(r)}$ characterized by

$$\mathbb{M}^{(r)} = \sum_{k=1}^{K} \frac{1}{2m^{(r,k)}} \boldsymbol{\mu}^{(r,k)} \otimes \boldsymbol{\mu}^{(r,k)} \quad \text{and} \quad \boldsymbol{\eta}^{(r)} = \sum_{k=1}^{K} \eta^{(r,k)} \boldsymbol{\mu}^{(r,k)} \tag{24}$$

with

$$\frac{1}{2m^{(r,k)}} = \frac{\hat{\gamma}^{(r,k)} - \check{\gamma}^{(r,k)}}{\hat{\tau}^{(r,k)} - \check{\tau}^{(r,k)}} \quad \text{and} \quad \eta^{(r,k)} = \check{\gamma}^{(r,k)} - \frac{\check{\tau}^{(r,k)}}{2m^{(r,k)}}. \tag{25}$$

In these last expressions, the various resolved stresses and slip rates depend on $\overline{\boldsymbol{\sigma}}_d$ and $\left\{\overline{\rho}^{(r,k)}\right\}$ through the first and second moments of the stress field within the grains; they can be written as

$$\hat{\tau}^{(r,k)} = \overline{\tau}^{(r,k)} + \sqrt{\overline{\overline{\tau}}^{(r,k)^2} - \overline{\tau}^{(r,k)^2}} \quad \text{and} \quad \check{\tau}^{(r,k)} = \overline{\tau}^{(r,k)} - \sqrt{\overline{\overline{\tau}}^{(r,k)^2} - \overline{\tau}^{(r,k)^2}}, \tag{26}$$

$$\hat{\gamma}^{(r,k)} = \dot{\gamma}^{(r,k)}\left(\hat{\tau}^{(r,k)}, \{\overline{\rho}^{(r,k)}\}\right) \quad \text{and} \quad \check{\gamma}^{(r,k)} = \dot{\gamma}^{(r,k)}\left(\check{\tau}^{(r,k)}, \{\overline{\rho}^{(r,k')}\}\right), \tag{27}$$

where

$$\overline{\tau}^{(r,k)} = \boldsymbol{\mu}^{(r,k)} \cdot \langle \boldsymbol{\sigma}_d \rangle^{(r)} \quad \text{and} \quad \overline{\overline{\tau}}^{(r,k)} = \sqrt{\boldsymbol{\mu}^{(r,k)} \cdot \langle \boldsymbol{\sigma}_d \otimes \boldsymbol{\sigma}_d \rangle^{(r)} \boldsymbol{\mu}^{(r,k)}}. \tag{28}$$

The local crystal plasticity law in this linear-comparison polycrystal is of the form $\dot{\gamma}^{(r,k)} = \boldsymbol{\sigma}_d \cdot \boldsymbol{\mu}^{(r,k)}/(2m^{(r,k)}) + \eta^{(r,k)}$. Thus, relations (25) constitute a secant linearization of the non-linear stress-slip-rate response of the crystals that incorporates intragranular stress statistics of up to second order through the standard deviations of the resolved shear stresses $SD^{(r,k)}(\tau) = (\overline{\overline{\tau}}^{(r,k)^2} - \overline{\tau}^{(r,k)^2})^{1/2}$, see fig. 2. These stress statistics can be computed from the effective properties of the linear-comparison polycrystal through the identities

$$\langle \boldsymbol{\sigma}_d \rangle^{(r)} = \frac{1}{c^{(r)}} \frac{\partial \widetilde{u}}{\partial \boldsymbol{\eta}^{(r)}} \quad \text{and} \quad \langle \boldsymbol{\sigma}_d \otimes \boldsymbol{\sigma}_d \rangle^{(r)} = \frac{2}{c^{(r)}} \frac{\partial \widetilde{u}}{\partial \mathbb{M}^{(r)}}, \tag{29}$$

where $\widetilde{u}$ is an effective stress potential of the linear-comparison polycrystal of the form

$$\widetilde{u}\left(\overline{\boldsymbol{\sigma}}_d, \{\mathbb{M}^{(r)}\}, \{\boldsymbol{\eta}^{(r)}\}\right) = \frac{1}{2}\overline{\boldsymbol{\sigma}}_d \cdot \widetilde{\mathbb{M}}\overline{\boldsymbol{\sigma}}_d + \widetilde{\boldsymbol{\eta}} \cdot \overline{\boldsymbol{\sigma}}_d + \frac{1}{2}\widetilde{g}. \tag{30}$$

The effective properties $\widetilde{\mathbb{M}}$, $\widetilde{\boldsymbol{\eta}}$ and $\widetilde{g}$ must be estimated by some suitable *linear* homogenization scheme for N-phase media. The so-called Self-Consistent scheme of Laws (1973) and Willis (1981) is known to be particularly suitable for polycrystalline media of the type considered in this work; expressions are recalled in Appendix A for convenience. Finally, the first and second moments of the intragranular slip rates can be computed as

$$\overline{\gamma}^{(r,k)} = \frac{\overline{\tau}^{(r,k)}}{2m^{(r,k)}} + \eta^{(r,k)} \quad \text{and} \quad \overline{\overline{\gamma}}^{(r,k)} = \sqrt{\frac{\overline{\overline{\tau}}^{(r,k)^2}}{4m^{(r,k)^2}} + \frac{\eta^{(r,k)}\ \overline{\tau}^{(r,k)}}{m^{(r,k)}} + \eta^{(r,k)^2}}. \tag{31}$$

Therefore, the mathematical structure of this second-order homogenization scheme suggests four natural choices for the slip-rate measures $\dot{\bar{\Gamma}}^{(r,k)}_{FOSO}$ dictating the evolution of dislocation densities: $|\overline{\gamma}^{(r,k)}|$, $|\check{\gamma}^{(r,k)}|$, $|\hat{\gamma}^{(r,k)}|$, and $\overline{\overline{\gamma}}^{(r,k)}$. Each choice generates a different set of predictions as discussed in Section 5 below. Note that the nonlinear local behavior of the grains enter the homogenization scheme only through relations (27) and evolution equations (18); the scheme is thus easily adapted to other types of local behaviors.

Evaluating the function (23) requires, therefore, the solution of a system of non-linear algebraic equations for the $2 \times N \times K$ linear-comparison local properties $m^{(r,k)}$ and $\eta^{(r,k)}$, coupled with the system of non-linear algebraic equations for the linear-comparison effective properties (A.5). Fixed-point methods are employed for that purpose in the present study. In turn, time integration of the evolution equations (18) is carried out by means of an implicit Euler scheme with fixed time stepping.

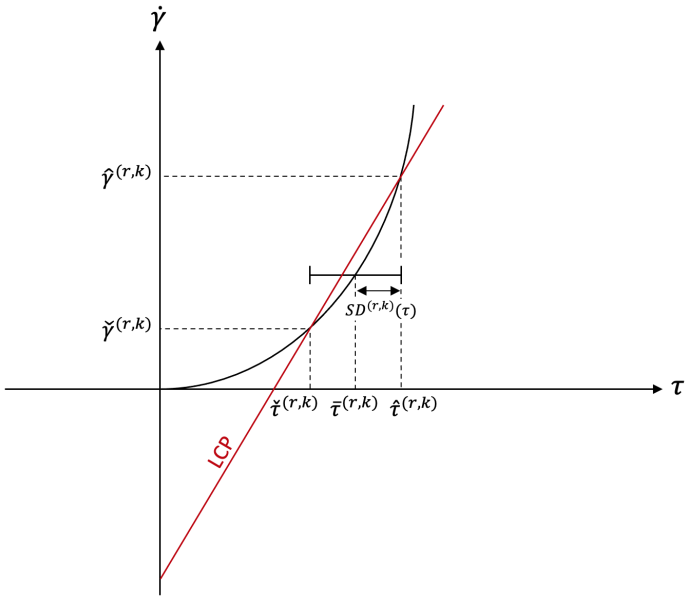

Figure 2: Schematic of the linearization employed by the second-order homogenization scheme of Ponte Castañeda (2015).

4.3. A simpler linear-comparison scheme of the Self-Consistent type

A simpler version of the above linear-comparison homogenization scheme is available from the earlier work of DeBotton and Ponte Castañeda (1995). This simpler scheme employs a secant linearization about the second moments of the intraphase stresses rather than the generalized-secant linearization (25) based on first and second moments. It approximates the function (17) by

$$\dot{\widetilde{\mathbf{E}}}_{SEC}\left(\overline{\boldsymbol{\sigma}}_d, \left\{\overline{\rho}^{(r,k)}\right\}\right) = \widetilde{\mathbb{M}}\left(\overline{\boldsymbol{\sigma}}_d, \left\{\overline{\rho}^{(r,k)}\right\}\right)\overline{\boldsymbol{\sigma}}_d, \tag{32}$$

where the tensor function $\widetilde{\mathbb{M}}$ is given by the Self-Consistent estimate (A.5) for the effective property of a linear-comparison polycrystal with the same microgeometry as the original polycrystal but with linear local responses of the form $\dot{\boldsymbol{\varepsilon}}_d = \mathbb{M}^{(r)}\boldsymbol{\sigma}_d$ with $\mathbb{M}^{(r)}$ characterized by the above formulae with $\check{\tau}^{(r,k)} = 0$ and $\hat{\tau}^{(r,k)} = \overline{\overline{\tau}}^{(r,k)}$. The dislocation densities can then be updated by identifying slip-rate measures $\overline{\Gamma}^{(r,k)}_{SEC}$ with $|\overline{\gamma}^{(r,k)}|$ as given by $(31)_1$.

5. Sample results and discussion

Sample results are reported for specimens subject to uniaxial tension under four different scenarios: (a) unirradiated specimens loaded at a low rate, (b) irradiated specimens loaded at a low rate, (c) unirradiated specimens loaded at a high rate, (d) irradiated specimens loaded at a high rate. Unirradiated specimens have no solute clusters so that $c_{SC} = 0$, while irradiated specimens have a solute cluster content $c_{SC} = 8.8 \times 10^{-2} c_{SC0}$ associated with a high fluence. In turn, the low and high loading rates are respectively $\dot{\overline{\sigma}}_e = \mu\dot{\varepsilon}_0$ and $\dot{\overline{\sigma}}_e = 100\mu\dot{\varepsilon}_0$, $\dot{\varepsilon}_0 = 2 \times 10^{10}\dot{\gamma}_0$ is a characteristic macroscopic strain rate. Henceforth, $\overline{\sigma}_e = \sqrt{(3/2)\overline{\boldsymbol{\sigma}}_d \cdot \overline{\boldsymbol{\sigma}}_d}$ and $\overline{\varepsilon}_e = \sqrt{(2/3)\overline{\boldsymbol{\varepsilon}}_d \cdot \overline{\boldsymbol{\varepsilon}}_d}$ denote the von Mises equivalent stress and strain, respectively. Initially, undeformed specimens are free of residual stresses and contain an equal amount of dislocation densities $\rho_{init} = 2.0 \times 10^{-2}\rho_0$ on all slip systems.

Full-field simulations for unirradiated specimens subject to uniaxial tension at low loading rate are shown in fig. 3. Traction curves in the form of equivalent stress versus equivalent strain, respectively normalized by τ_{cr} and $\gamma_{cr} = \tau_{cr}/\mu$, together with the concomitant evolution of total dislocation density, normalized by its

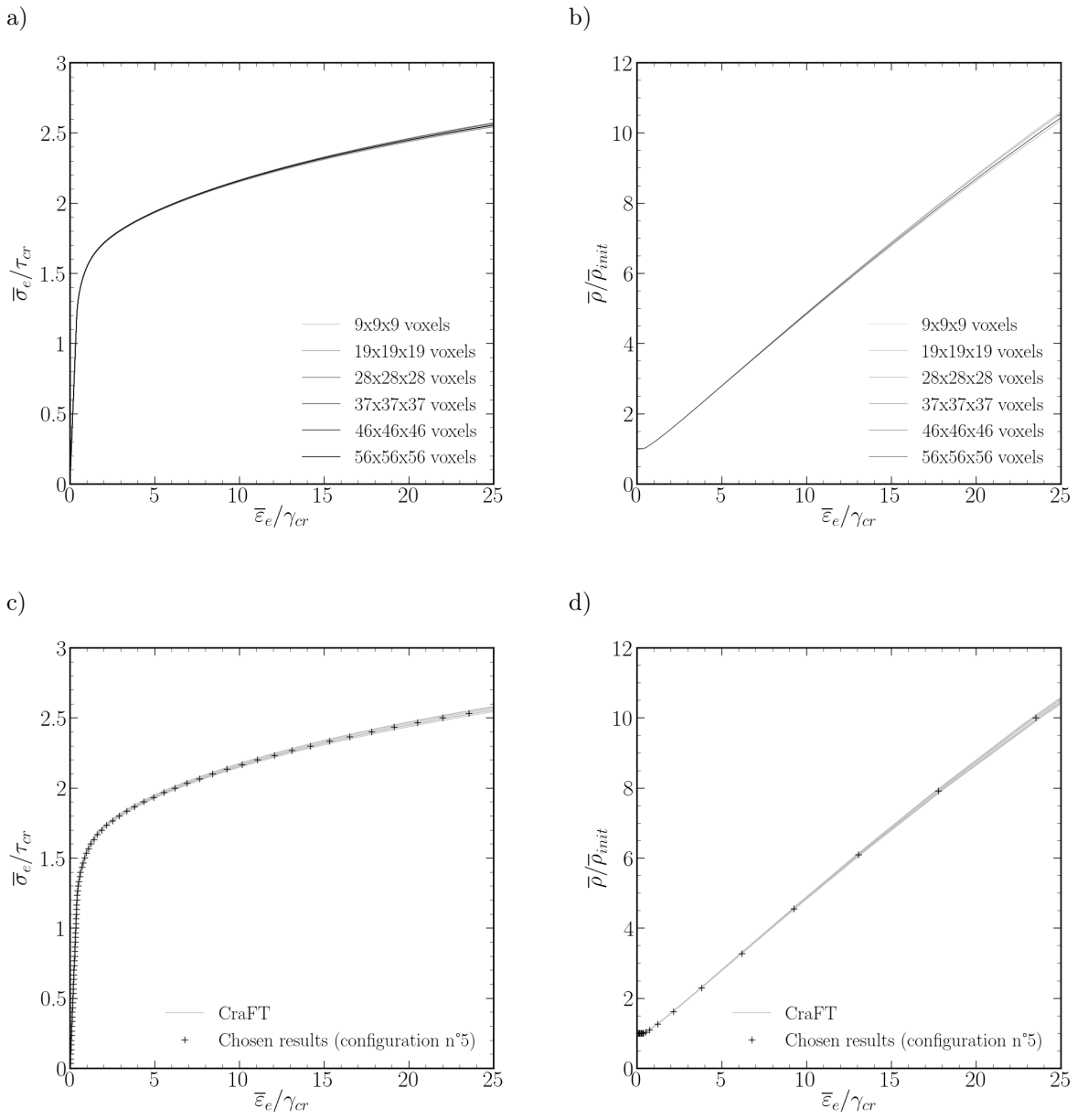

Figure 3: Full-field simulations for unirradiated specimens subject to uniaxial tension at low loading rate: (a) traction curves and (b) total dislocation densities for a single realization discretized with 9^3, 19^3, 28^3, 37^3, 47^3, and 56^3 voxels per unit cell; (c) traction curves and (d) total dislocation densities for ten realizations discretized with 47^3; symbols correspond to the most representative realization.

initial value $\overline{\rho}_{init} = 12\rho_{init}$, are displayed in parts (a) & (b) for the first realization of fig. 1 discretized with 9^3 (2^3), 19^3 (4^3), 28^3 (6^3), 37^3 (8^3), 47^3 (10^3), and 56^3 (12^3) voxels per unit cell (per grain), respectively. Convergence tolerances of 10^{-3} were required on equilibrium and loading conditions. A weak sensitivity to discretization is observed. It is concluded that 47^3 voxels per unit cell suffices for the purposes of this study. Corresponding curves are thus displayed in parts (c) & (d) for the ten realizations of fig. 1, discretized with 47^3 voxels. The spread among responses is seen to be quite small. Thus, the most representative realization of the ensemble is identified and exclusively considered in the comparisons henceforth.

Traction curves for the four scenarios are displayed in fig. 4. In turn, the slopes of these curves and the concomitant evolutions of total dislocation density are displayed in figs. 5 and 6, respectively. The second-order (FOSO) homogenization scheme is compared with the elementary homogenization schemes of Sachs and Taylor along with the full-field simulations (FFT). We begin by noting that full-field simulations exhibit traction curves with pronounced elastoplastic transitions and subsequent plastic hardening. Stresses at which elastoplastic transitions occur show an appreciable increase with loading rate and radiation dose, while plastic hardening rates deep in the plastic range show a similar trend albeit of weaker magnitude. Plastic flow is seen to be accompanied by a pronounced non-convex growth of dislocation densities. This growth becomes approximately linear with overall deformation deep in the plastic range, and is faster under radiation but quite indifferent to loading rate, at least when evaluated versus macroscopic deformation. Relative to these numerically exact predictions, approximate mean-field predictions delivered by the elementary schemes of Sachs and Taylor are seen to be quite inaccurate. It is recalled that, for certain classes of constitutive laws, these elementary schemes deliver lower and upper bounds on the macroscopic flow stress, and the gap between the bounds can be regarded as a measure of local constitutive heterogeneity (e.g., Ponte Castañeda and Suquet, 1998). In the present context, elementary estimates differ appreciably not only in terms of the initial flow stresses but also in terms of the plastic hardening rates. Thus, differences between the predicted flow stresses intensify with deformation. Interestingly, the hardening rates exhibited by the Taylor bound can evolve non-monotonically during the elastoplastic transition. This non-monotonocity could be ascribed to the presence of an 'apparent' macroscopic hardening associated with microstructural heterogeneity alongside the strain hardening associated with the evolution of dislocation densities. The Sachs bound, by contrast, does not incorporate an apparent hardening due to the assumed uniformity of the underlying stress field and therefore exhibits a monotonically decreasing slope in all cases. Similar trends are observed in the corresponding estimates for the total dislocation densities. To further assess the need of refined schemes to properly describe these material systems, figs. 4a & 6a also display predictions generated by the secant linear-comparison scheme (SEC) of Section 4.3. It is recalled that, for certain classes of constitutive laws, this scheme delivers upper bounds on the flow stresses predicted by any other linear-comparison scheme of the Self-Consistent type (e.g., Ponte Castañeda and Suquet, 1998). This is the reason why the resulting predictions are closer to those of the Taylor scheme than to those of the full-field descriptions. Similar trends result from the use of the first-order homogenization scheme of Berveiller and Zaoui (1978) as reported by Monnet et al. (2019). The potential benefits of a refined, albeit more complicated, second-order homogenization scheme are therefore evident.

Song and Ponte Ponte Castañeda (2018) found that the second-order homogenization scheme of Section 4.2 can reproduce full-field simulations for the viscoplastic flow of hexagonal polycrystals quite accurately. Previous works such as that of Lebensohn et al. (2007) had already found an earlier version of this second-order scheme capable of reproducing full-field simulations for the viscoplastic flow of hexagonal as well as cubic polycrystals. In line with those findings, the most accurate predictions for all scenarios considered in the present context are seen indeed to be those generated by that second-order homogenization scheme, regardless of the choice of slip-rate measure employed for the evolution of dislocation densities. We refer to the four variants of these second-order estimates as FOSO($\overline{\gamma}$), FOSO($\breve{\gamma}$), FOSO($\hat{\gamma}$) and FOSO($\overline{\overline{\gamma}}$), see Section 4.2. These variants are seen to be indistinguishable during the elastic response and the initial elastoplastic transition, but are seen to diverge from one another as plastic deformations develop. In fact, the FOSO($\overline{\gamma}$) and FOSO($\overline{\overline{\gamma}}$) estimates exhibit non-monotonic hardening rates like the Taylor bound, while the FOSO($\breve{\gamma}$), FOSO($\hat{\gamma}$) estimates exhibit monotonic hardening rates like the FFT results. Interestingly, their relative merits depend on the standpoint adopted. The FOSO($\overline{\gamma}$) estimates based on standard first-order intra-granular statistics delivers the most accurate predictions for the macroscopic flow stress deep in the plastic

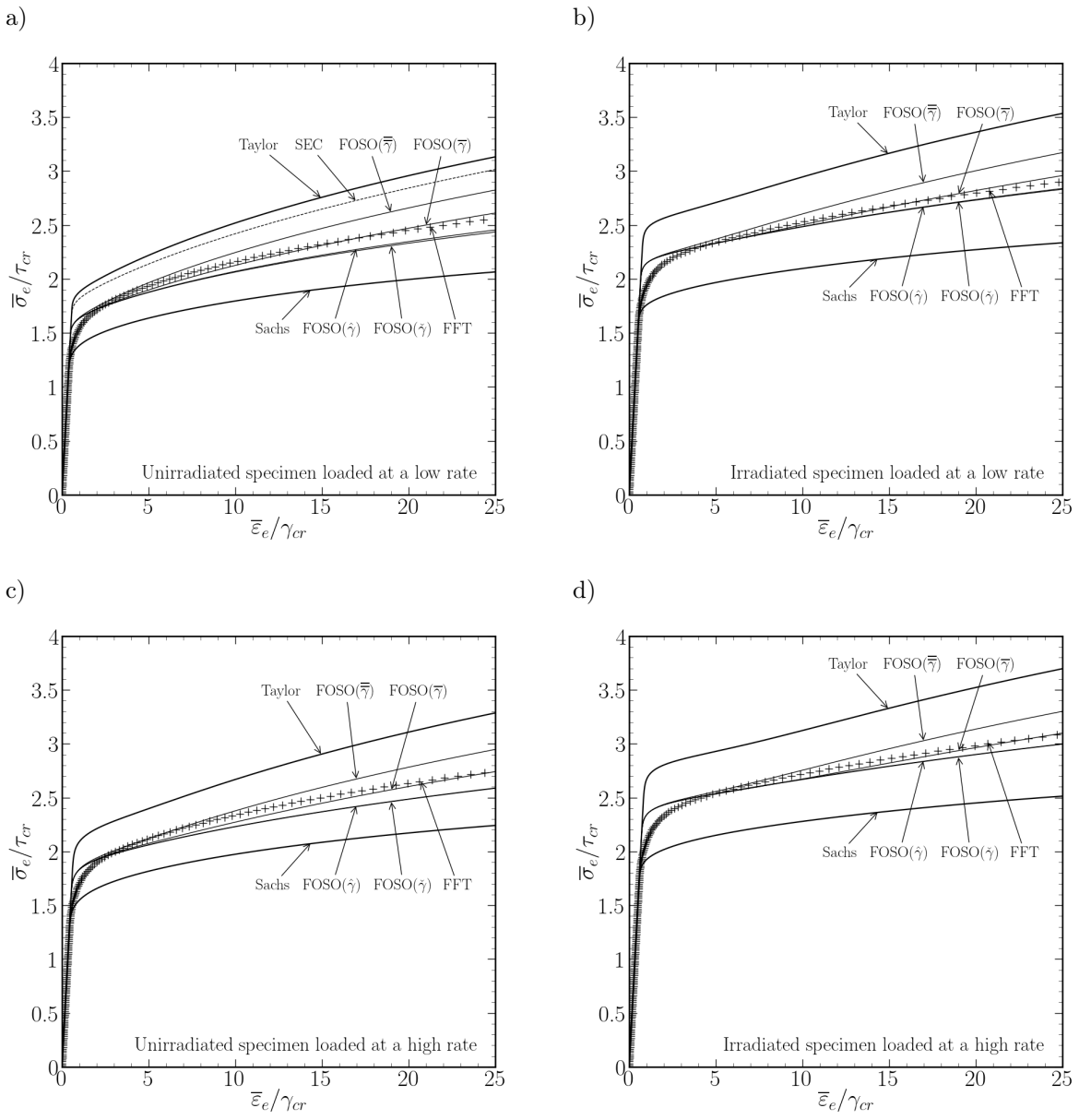

Figure 4: Traction curves for: (a) unirradiated specimens loaded at a low rate, (b) irradiated specimens loaded at a low rate, (c) unirradiated specimens loaded at a high rate, (d) irradiated specimens loaded at a high rate. Full-field simulations (FFT) are compared with elementary homogenization schemes of the Sachs and Taylor types, and the second-order (FOSO) homogenization scheme of the Self-Consistent type. Also included in part (a) is the secant (SEC) homogenization scheme of the Self-Consistent type.

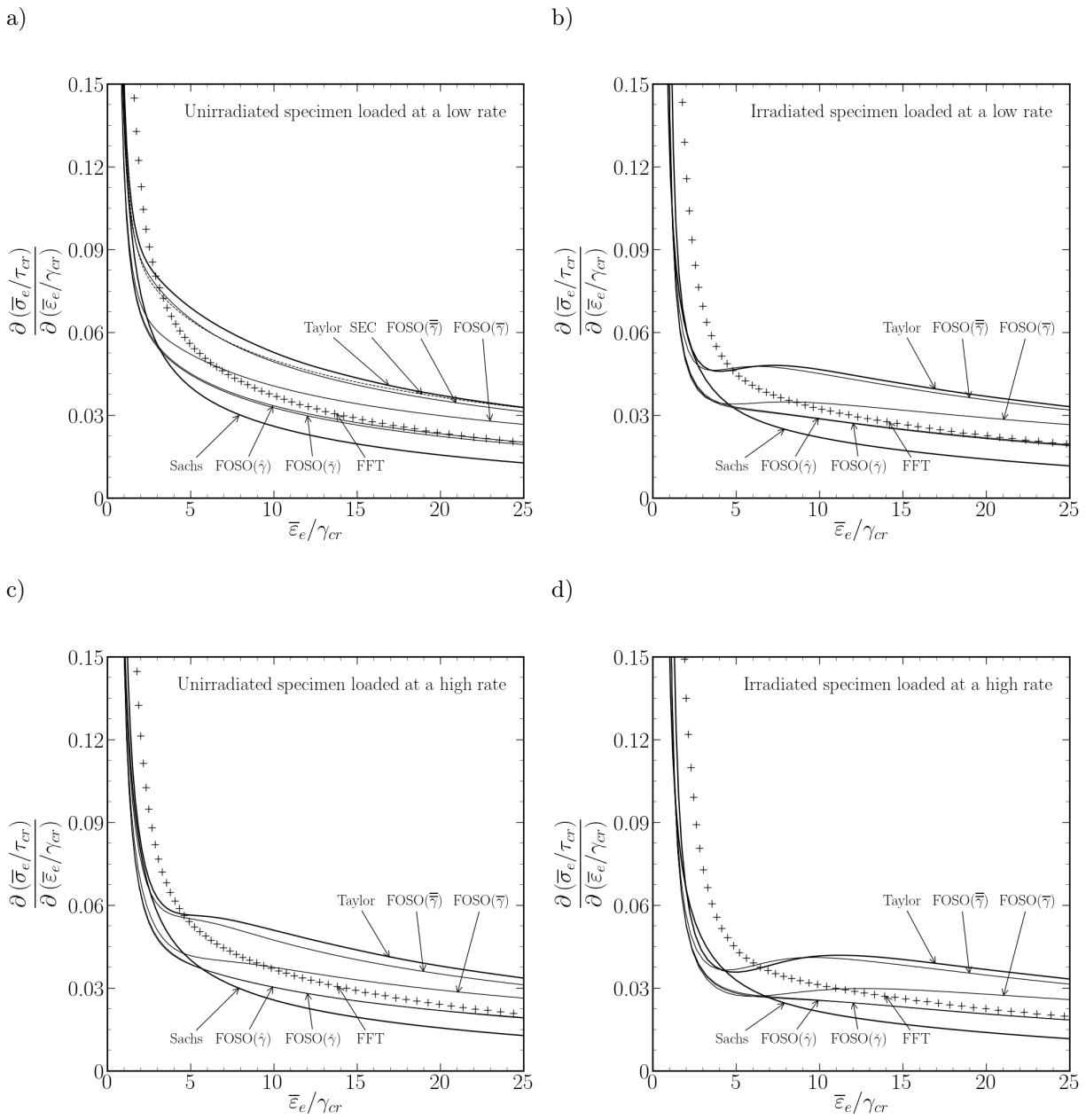

Figure 5: Slopes of traction curves for: (a) unirradiated specimens loaded at a low rate, (b) irradiated specimens loaded at a low rate, (c) unirradiated specimens loaded at a high rate, (d) irradiated specimens loaded at a high rate. Full-field simulations (FFT) are compared with elementary homogenization schemes of the Sachs and Taylor types, and the second-order (FOSO) homogenization scheme of the Self-Consistent type.

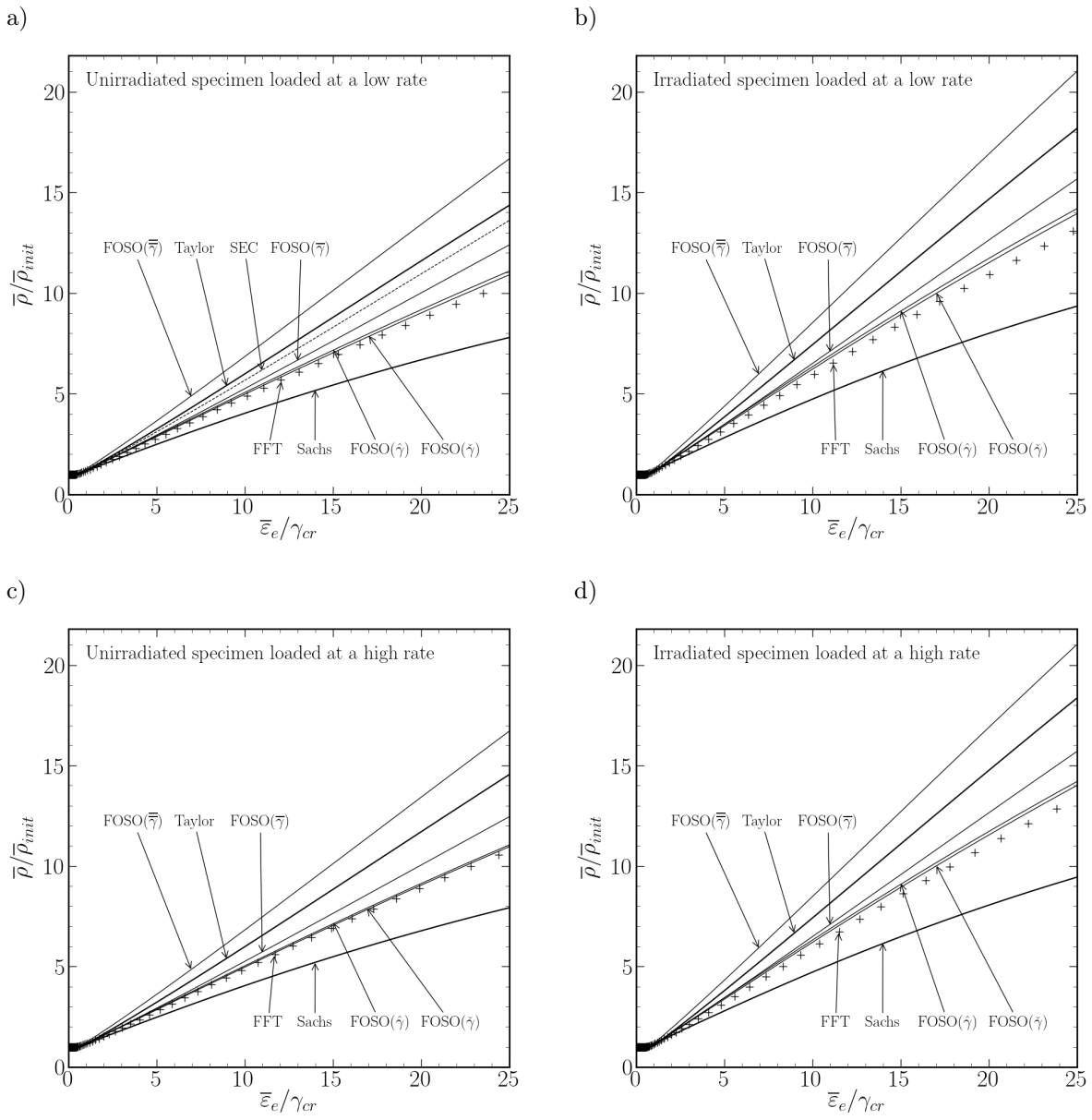

Figure 6: Total dislocation densities, normalized by its initial value, for: (a) unirradiated specimens loaded at a low rate, (b) irradiated specimens loaded at a low rate, (c) unirradiated specimens loaded at a high rate, (d) irradiated specimens loaded at a high rate. Full-field simulations (FFT) are compared with elementary homogenization schemes of the Sachs and Taylor types, and the second-order (FOSO) homogenization scheme of the Self-Consistent type.

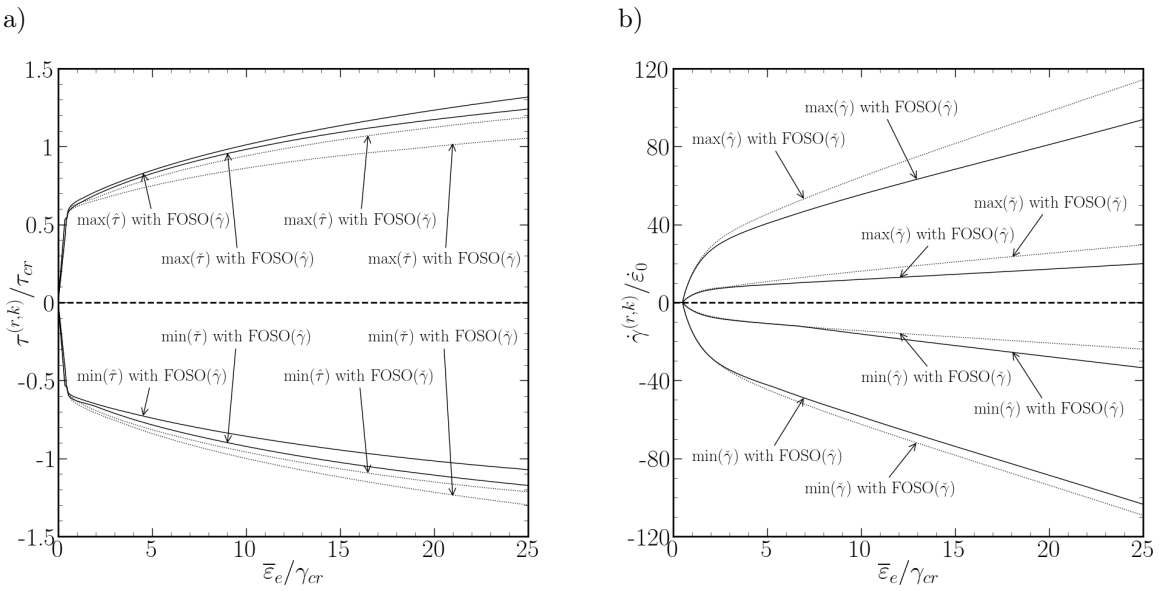

Figure 7: Maximum and minimum values among all (a) resolved stresses and (b) slip rates employed by the FOSO($\check{\gamma}$) (continuous lines) and FOSO($\hat{\gamma}$) (dotted lines) estimates in unirradiated specimens loaded at a low rate.

range, at least for the range of deformations considered. However, this is probably due to a compensation of inaccuracies. Indeed, all second-order estimates overestimate flow stresses in the elastoplastic transition as a consequence of the decoupled homogenization of elastic and plastic deformations. The FOSO($\overline{\gamma}$) estimates compensate this overestimation with the peculiar evolution of the plastic hardening rate. By contrast, the alternative FOSO($\check{\gamma}$) and FOSO($\hat{\gamma}$) estimates based on intragranular slip rate fluctuations deliver somewhat less accurate predictions for the flow stress but the most accurate predictions for the plastic hardening rate deep in the plastic range. Thus, this accurate hardening rate does not compensate the inaccuracies induced on flow stresses by the elastoplastic decoupling. From a practical standpoint prioritizing accuracy of flow stresses, FOSO($\overline{\gamma}$) estimates appear to be preferable; from a theoretical standpoint, however, the alternative FOSO($\check{\gamma}$) and FOSO($\hat{\gamma}$) estimates should be regarded as most befitting. If combined with a coupled homogenization of elastic and plastic deformations (e.g., Lahellec and Suquet, 2013; Das and Ponte Castañeda, 2021), the alternative choices $\check{\gamma}$ and $\hat{\gamma}$ for updating dislocation densities are likely to generate the most accurate predictions. In fact, these alternative estimates are already seen to deliver the most accurate predictions for the total dislocation density within the entire range of loading rates and radiation doses considered. Figure 7 shows plots for the maximum and minimum values among all resolved stresses ($\{\check{\tau}^{(r,k)}\}, \{\hat{\tau}^{(r,k)}\}$) and slip rates ($\{\check{\gamma}^{(r,k)}\}, \{\hat{\gamma}^{(r,k)}\}$) associated with the FOSO($\check{\gamma}$) and FOSO($\hat{\gamma}$) estimates in unirradiated specimens loaded at a low rate. An approximately specular symmetry about zero is observed between the two sets of curves. This is a consequence of the opposing signs in the definitions (26) for the resolved stresses $\check{\tau}^{(r,k)}$ and $\hat{\tau}^{(r,k)}$, and, together with the fact that dislocation density rates are proportional to the absolute values $|\check{\gamma}^{(r,k)}|$ or $|\hat{\gamma}^{(r,k)}|$, it explains the similitudes between predictions generated by the two types of estimates. Finally, the FOSO($\overline{\overline{\gamma}}$) estimates based on the second moments of the intragranular slip rates are seen to be the least accurate among the second-order estimates: they overestimate plastic hardening rate and therefore flow stresses deep in the plastic range, and significantly overestimate the total dislocation density, even in excess of the Taylor estimates. Additional comparisons have also been performed with an alternative set of material parameters corresponding to higher subfreezing temperatures. The FOSO($\check{\gamma}$) and FOSO($\hat{\gamma}$) estimates are found to outperform the other estimates even more notably, providing accurate predictions not only for the hardening rates but also for the flow stresses (Chaix, 2023). It is noted, however, that the most relevant choice of slip-rate measures for the description of hardening may be contingent on the specific crystal plasticity law. For instance, Suquet and Lahellec (2014) have advocated

for the use of the second moments of intragranular plastic slip and have verified its suitability for certain crystal plasticity laws describing transient creep in ice. On the other hand, Castelnau et al. (2006) reported mean-field descriptions of the self-consistent type for two-dimensional model polycrystals exhibiting linearly viscous slip rates with linearly hardening flow stresses and observed that the predicted stress-strain response was relatively insensitive to the use of slip-rate measures employing statistical information beyond the first moments. It would not be surprising that higher-order slip-rate measures may result progressively more relevant as the crystal plasticity law is increasingly nonlinear.

In conclusion, second-order homogenization estimates based on a generalized-secant linearization are found to provide an appropriate compromise between precision and mathematical complexity to generate mean-field descriptions for the elastoplastic response of polycrystalline media governed by complex crystal plasticity laws. Most accurate descriptions should result from the combined use of a generalized-secant linearization of the crystal plasticity law, a slip-rate measure incorporating information on intragranular slip-rate fluctuations for the evolution of the dislocation densities, and a coupled homogenization of the elastic and plastic deformations. Strategies to incorporate this last feature in the above mean-field descriptions for neutron-irradiated bainitic steels are currently under investigation.

Acknowledgments

The work was funded by the Institute of Fusion and Instrumentation Sciences in Nuclear Environments (ISFIN) and by the Institut de Radioprotection et de Sûreté Nucléaire (IRSN). Additional funds from the Universidad Nacional de La Plata (UNLP) were recieved by M.I.I. through grant I-2019-247.

References

Berveiller, M., Zaoui, A., 1978. An extension of the self-consistent scheme to plastically-flowing polycrystals. J. Mech. Phys. Solid. 26, 325–344.

Bornert, M., Ponte Castañeda, P., 1998. Second-order estimates of the Self-Consistent type for viscoplastic polycrystals. Proc. R. Soc. Lond. A 454, 3035–3045.

Castelnau, O., Brenner, R., Lebensohn, R.A., 2006. The effect of strain heterogeneity on the work hardening of polycrystals predicted by mean-field approaches. Acta Mater. 54, 2745–2756.

Chaix, L., 2023. Modélisation micromécanique du comportement viscoplastique d'un polycristal. Report IRSN/2022-00588.

Chakraborty, P., Biner, B., 2014. A unified cohesive zone approach to model the ductile to brittle transition of fracture toughness in reactor pressure vessel steels. Engng. Fract. Mech. 131, 194–209.

Das, S., Ponte Castañeda, P., 2021. Differential variational estimates for the macroscopic response and field statistics of elasto-viscoplastic polycrystals. J. Mech. Phys. Solids 147, 104202.

DeBotton, G., Ponte Castañeda, P., 1995. Variational estimates for the creep behaviour polycrystals. Proc. R. Soc. Lond. A 448, 121–142.

Dendievel, R., Bonnet, G., Willis, J.R., 1990. Bounds for the creep behaviour polycrystalline materials. In Inelastic deformation of composite materials (ed. G.J. Dvorak), pp. 175–192. New York, NY: Springer.

Idiart, M.I., Lahellec, N., 2016. Estimates for the overall linear properties of pointwise heterogeneous solids with application to elasto-viscoplasticity. J. Mech. Phys. Solids 97, 317–332.

Kocks, U.F., Mecking, H. 2003. Physics and phenomenology of strain hardening: the FCC case. Prog. Mater. Sci. 48, 171–273.

Lahellec, N., Suquet, P., 2013. Effective response and field statistics in elasto-plastic and elasto-viscoplastic composites under radial and non-radial loadings. Int. J. Plasticity 42, 1–30.

Laws, N., 1973. On the thermostatics of composite materials. J. Mech. Phys. Solids 21, 9–17.

Lebensohn, R.A., Tomé, C.N., Ponte Castañeda, P., 2007. Self-consistent modelling of the mechanical behaviour of viscoplastic polycrystals incorporating intragranular field fluctuations. Phil. Mag. 87, 4287–4322.

Lebensohn, R.A., Idiart, M.I., Ponte Castañeda, P., Vincent, P.-G., 2011. Dilatational viscoplasticity of polycrystalline solids with intergranular cavities. Phil. Mag. 91, 3038–3067.

Liu, Y., 2003. Macroscopic Behavior, Field Fluctuations and Texture Evolution in Viscoplastic Polycrystals. Ph.D. thesis. University of Pennsylvania.

Liu, Y., Ponte Castañeda, P., 2004. Second-order theory for the effective behavior and field fluctuations in viscoplastic polycrystals. J. Mech. Phys. Solids 52, 467–495.

Masson, R., Bornert, M., Suquet, P., Zaoui, A., 2000. An affine formulation for the prediction of the effective properties of nonlinear composites and polycrystals. J. Mech. Phys. Solids 48, 1203–1227.

Michel, J.C., Suquet, P. 2004. Computational analysis of nonlinear composite structures using the nonuniform transformation field analysis. Comput. Methods Appl. Mech. Engrg. 193, 5477–5502.

Monnet, G., Vincent, L., Gélébart, L. 2019. Multiscale modeling of crystal plasticity in Reactor Pressure Vessel steels: Prediction of irradiation hardening. J. Nuclear Mater. 514, 128–138.

Moulinec, H., Suquet, P. 1994. A fast numerical method for computing the linear and nonlinear properties of composites. C. R. Acad. Sci. Paris II 318, 1417–1423.
Moulinec, H., Suquet, P. 1998. A numerical method for computing the overall response of nonlinear composites with complex microstructure. Computer Methods in Applied Mechanics and Engineering, 69–94.
Ponte Castañeda, P., 2015. Fully optimized second-order variational estimates for the macroscopic response and field statistics in viscoplastic crystalline composites. Proc. R. Soc. A 471, 20150665.
Ponte Castañeda, P., Suquet, P., 1998. Nonlinear composites. Adv. Appl. Mech. 34, 171–302.
Segurado, J., Lebensohn, R., Llorca, J., 2018. Computational homogenization of polycrystals. Adv. Appl. Mech. 51, 1–114.
Song, D., Ponte Castañeda, P. 2018. Fully optimized second-order homogenization estimates for the macroscopic response and texture evolution of low-symmetry viscoplastic polycrystals. Int. J. Plast. 110, 272–293.
Suquet, P., Lahellec, N., 2014. Elasto-plasticity of heterogeneous materials at different scales. Procedia IUTAM 10, 247–262.
Willis, J.R. 1981. Variational and related methods for the overall properties of composites. Adv. Appl. Mech. 21, 1–78.
Willis, J.R. 1983. The overall elastic response of composite materials. J. Appl. Mech. 50, 1202–1209.
Zecevic, M., Lebensohn, R.A., 2020. New robust self-consistent homogenization schemes of elasto-viscoplastic polycrystals. Int. J. Solids Struct. 202, 434–453.

Appendix A. The Self-Consistent scheme

Self-consistent estimates for thermoelastic systems are available from the works of Laws (1973) and Willis (1981). They can be written as

$$\widetilde{\mathbb{M}} = \sum_{r=1}^{N} c^{(r)} \mathbb{M}^{(r)} \mathbb{B}^{(r)}, \quad \widetilde{\boldsymbol{\eta}} = \sum_{r=1}^{N} c^{(r)} {\mathbb{B}^{(r)}}^{T} \boldsymbol{\eta}^{(r)}, \quad \text{and} \quad \widetilde{g} = \sum_{r=1}^{N} c^{(r)} \mathbf{b}^{(r)} \cdot \boldsymbol{\eta}^{(r)}, \tag{A.1}$$

where $\mathbb{B}^{(r)}$ and $\mathbf{b}^{(r)}$ are concentration tensors given by

$$\mathbb{B}^{(r)} = \left(\mathbb{M}^{(r)} + \widetilde{\mathbb{M}}^{*}\right)^{-1} \left(\widetilde{\mathbb{M}} + \widetilde{\mathbb{M}}^{*}\right) \quad \text{and} \quad \mathbf{b}^{(r)} = \left(\mathbb{M}^{(r)} + \widetilde{\mathbb{M}}^{*}\right)^{-1} \left(\widetilde{\boldsymbol{\eta}} - \boldsymbol{\eta}^{(r)}\right). \tag{A.2}$$

In this last expression, $\widetilde{\mathbb{M}}^{*} = \widetilde{\mathbb{Q}}^{-1} - \widetilde{\mathbb{M}}$ where $\widetilde{\mathbb{Q}}$ is a microstructural tensor that depends on $\widetilde{\mathbb{M}}$ and on the 'shape' of the two-point correlation functions for the distribution of the grain orientations. The polycrystals considered in this work are 'equi-axed' and untextured so that the two-point correlation functions exhibit isotropic symmetry. In this case,

$$\widetilde{\mathbb{Q}} = \widetilde{\mathbb{L}} - \widetilde{\mathbb{L}}\widetilde{\mathbb{P}}\widetilde{\mathbb{L}} \quad \text{with} \quad \widetilde{\mathbb{P}} = \frac{1}{4\pi} \int_{|\boldsymbol{\xi}|=1} \widetilde{\mathbb{H}}(\boldsymbol{\xi}) \, \mathrm{d}S, \tag{A.3}$$

where $\widetilde{\mathbb{L}} = \widetilde{\mathbb{M}}^{-1}$, and the components of $\widetilde{\mathbb{H}}(\boldsymbol{\xi})$ are given in terms of the components of the accoustic tensor $\widetilde{K}_{ik} = \widetilde{L}_{ijkl}\xi_j\xi_l$ by

$$\tilde{H}_{klmn} = \widetilde{K}^{-1}_{km} \, \xi_l \, \xi_n - \left. \frac{\widetilde{K}^{-1}_{ko}\widetilde{K}^{-1}_{mp} \, \xi_o \, \xi_p \, \xi_l \, \xi_n}{\xi_a \widetilde{K}^{-1}_{ab} \xi_b} \right|_{(kl)(mn)}. \tag{A.4}$$

Finally, $\widetilde{\mathbb{M}}$ solves the implicit equation

$$\left(\widetilde{\mathbb{M}} + \widetilde{\mathbb{M}}^{*}\right)^{-1} = \sum_{r=1}^{N} c^{(r)} \left(\mathbb{M}^{(r)} + \widetilde{\mathbb{M}}^{*}\right)^{-1}, \tag{A.5}$$

which follows from the combination of expressions $(A.1)_1$ and $(A.2)_1$. In all the above expressions, the inverse of fourth-order tensors is defined in the subset of incompressible compliance tensors. Expressions for the derivatives required by the identities (29) can be found in Liu (2003).